Nanoscale

PAPER

View Article Online
View Journal | View Issue

Cite this: *Nanoscale*, 2020, **12**, 12531

Controlled growth and ion intercalation mechanism of monocrystalline niobium pentoxide nanotubes for advanced rechargeable aluminum-ion batteries†

Lei Wang,‡[a] Huinan Lin,‡[a] Weihua Kong,[a] Yi Hu,[a] Renpeng Chen,[a] Peiyang Zhao,[a] Mohammadreza Shokouhimehr,[b] Xiao Li Zhang,[c] Zuoxiu Tie[a] and Zhong Jin *[a,d]

Received 10th March 2020,
Accepted 2nd May 2020

DOI: 10.1039/d0nr01981j

rsc.li/nanoscale

Rechargeable aluminum-ion batteries (RAIBs) have attracted increasing attention owing to their high theoretical volumetric capacity, high resource abundance, and good safety performance. However, the existing RAIB systems usually exhibit relatively low specific capacities limited by the cathode materials. In this study, we developed a one-step chemical vapor deposition method to prepare single-crystal orthogonal Nb_2O_5 nanotubes for serving as high-performance electrode materials for RAIBs, showing a high reversible capability of 556 mA h g^{-1} at 25 mA g^{-1} and good thermal endurability at elevated temperatures (50 °C). A combination of a series of detailed *ex situ* structural characterization studies verified the reversible intercalation/deintercalation of chloroaluminate anions ($AlCl_4^-$) into/from the (001) planes of monocrystalline Nb_2O_5 nanotubes. It also revealed that the nanoarchitecture of Nb_2O_5 nanotubes with thin tube walls, hollow inner space and a short ion transport distance is conducive to the rapid kinetics of the insertion/extraction process. This work provides a promising route to design high-performance electrode materials based on transition metal compounds for RAIBs *via* the rational modulation of their structure and morphology.

1. Introduction

Owing to the rapid development of portable electronic devices, electric vehicles and smart power grid systems, the worldwide demand for advanced energy storage technology is ever-growing.[1–4] Currently, lithium-ion batteries (LIBs) are regarded as one of the most important mainstream products in the battery market.[5–8] However, the sustainable application of LIBs is restricted by the uneven distribution and shortage of lithium mineral resource.[9,10] Therefore, great efforts have been made to develop alternative secondary batteries based on non-lithium metals, such as sodium-ion batteries (SIBs),[11,12] magnesium-ion batteries,[13–15] zinc-ion batteries,[16–18] potassium-ion batteries[19,20] and calcium-ion batteries.[21,22] Among them, rechargeable aluminum-ion batteries (RAIBs) that rely on the electrochemical redox reactions of trivalent Al species possess several distinctive merits compared to other multivalent-ion batteries. Firstly, Al is the third most abundant element and the most abundant metal element in the Earth's crust;[23] the mature aluminum mining industry can tremendously lower the cost of RAIBs. Secondly, the three-electron process of the Al^{3+}/Al redox pair leads to an ultrahigh theoretical specific capacity (2980 A h kg^{-1}) and volumetric capacity (8046 A h L^{-1}). Moreover, the low flammability, low toxicity and high stability of the Al metal electrode make RAIBs relatively safe, and thus they have attracted broad attention and research interest in academia.

To prevent the large overpotential, high corrosion and hydrogen evolution of the Al electrode in aqueous electrolytes, non-aqueous electrolytes based on anhydrous $AlCl_3$ solution in ionic liquids, such as 1-ethyl-3-methylimidazolium chloride ([EMIm]Cl) or 1-butyl-3-methylimidazolium chloride ([BMIm]Cl), are usually employed in RAIBs.[24–51] Considering that the anode of RAIBs is normally Al metal foil, it is known that the cathode material acts as the key component to realize high

[a]*Key Laboratory of Mesoscopic Chemistry of MOE, School of Chemistry and Chemical Engineering, Nanjing University, Nanjing, Jiangsu 210023, China. E-mail: zhongjin@nju.edu.cn*
[b]*Department of Materials Science and Engineering, Research Institute of Advanced Materials, Seoul National University, Seoul 08826, Republic of Korea*
[c]*School of Materials Science and Engineering, Zhengzhou University, Zhengzhou 450001, China*
[d]*Shenzhen Research Institute of Nanjing University, Shenzhen 518063, China*
†Electronic supplementary information (ESI) available. See DOI: 10.1039/d0nr01981j
‡These authors contributed equally to this work.

power and energy densities. Previous research on the development of cathode materials for RAIBs can be classified into several different categories, including carbonaceous materials (such as graphite,[24–26] fluorinated graphite,[27] graphene,[28,29] 3D graphitic foam and graphene foam[30–32]), inorganic compounds (such as transition metal oxides[33–37] and transition metal sulfides[38–42]) and conducting polymers.[43–47] In 2015, Dai's group utilized 3D graphitic foam as the cathode material for RAIBs, which could work for over 7500 cycles at 4000 mA g^{-1}.[30] However, the state-of-the-art RAIBs usually suffer from poor specific capacity, owing to the intrinsic capacity limits of cathode materials. To improve the energy density of RAIBs, great efforts have been made on non-carbon materials like sulfur,[48–50] iodine[51] and transition metal chalcogenides.[33–42]

Among transition metal oxides, Nb_2O_5 is regarded as one of the potential electrode materials for LIBs, SIBs and supercapacitors,[52–59] owing to its adjustable morphologies, controllable crystallinity and ease of preparation. When used as the anode material for LIBs, Nb_2O_5 exhibits anomalously rapid Li^+-ion storage properties,[61–64] suggesting that its crystal structure may also be suitable for the high-rate intercalation/deintercalation of multivalent metal ions. However, the redox behavior and energy storage mechanism of Nb_2O_5 in RAIBs are yet to be explored, and the possible effect of structural modulation is unclear.

In this work, we developed a one-step chemical vapor deposition (CVD) method to prepare monocrystalline Nb_2O_5 nanotubes, and systematically investigated their electrochemical performance as an electrode material for RAIBs. Structural characterization demonstrated that the dominant exposed facets of single-crystal Nb_2O_5 nanotubes are the (001) planes with a lattice distance of 0.393 nm, which would be suitable for the insertion of tetrachloroaluminate ions ($AlCl_4^-$). Moreover, compared to commercial Nb_2O_5 powder, the nanostructural morphology features of Nb_2O_5 nanotubes with thin tube walls, hollow inner spaces and high porosity provide a shorter diffusion distance for the transport of charge carriers, leading to superior ion insertion/extraction rates. Benefiting from the above advantageous structural characteristics, RAIBs based on the electrodes of Nb_2O_5 nanotubes can deliver an ultrahigh specific capacity (556 mA h g^{-1} at 25 mA g^{-1}) and stable cycle life at 25 °C. Notably, even at an elevated temperature of 50 °C, the assembled RAIBs can still achieve a relatively high capacity of ~213 mA h g^{-1} after 30 cycles at 100 mA g^{-1}, indicating their remarkable thermal tolerance. A series of *ex situ* structural and compositional characterization studies confirmed that the energy storage mechanism of Nb_2O_5 nanotubes in RAIBs should be attributed to the reversible intercalation/deintercalation of $AlCl_4$ ions into the (001) planes of Nb_2O_5 crystal lattices.

2. Experimental section

2.1. CVD growth of Nb_2O_5 nanotubes

Briefly, 2 g of anhydrous $NbCl_5$ was used as the sole precursor and placed in a quartz boat inside an argon-filled glovebox and enclosed using a sealed packet. Then the quartz boat was rapidly transferred from the sealed packet to the central zone of a quartz tube furnace (with 1 inch diameter), as shown in Fig. 1a. The tube furnace was heated at 600 °C with a ramping rate of 5 °C min^{-1} under a dry air flow (50 sccm) and kept for 4 h. Then, the tube furnace was cooled to room temperature, and the as-prepared Nb_2O_5 nanotubes were collected from the non-heating zone at the downstream of the quartz tube.

2.2. Characterization

The morphology and structure of Nb_2O_5 nanotubes and commercial Nb_2O_5 powder were examined by SEM and HAADF-STEM analysis using an FEI Nova NanoSEM 450 instrument equipped with a Bruker X-flash 6|30 EDS accessory. TEM and SAED were performed with a JEOL JEM-2100 apparatus at 200 kV. Powder X-ray diffraction (XRD) data were collected on a Shimadzu LabX XRD-6000 instrument with a Cu Kα radiation source (λ = 1.54178 Å) in the 2θ angular range of 10–80°. Raman analysis was performed on a Horiba JY Evolution Raman spectrometer using a 633 nm laser source. X-ray photoelectron spectroscopy (XPS) was conducted on a PHI-5000 VersaProbe X-ray photoelectron spectrometer using an Al Kα X-ray source.

2.3. Electrochemical measurement

The electrodes were prepared by mixing 80 wt% of Nb_2O_5 nanotubes with 10 wt% of polyvinylidene fluoride (PVDF) binder (Sigma-Aldrich) and 10 wt% of acetylene black in *N*-methyl-2-pyrrolidinone (NMP) solvent (Sigma-Aldrich, 99.5%) to form a homogeneous slurry. The slurry was cast onto a Mo foil (1.0 mm thick) as a current collector with an areal loading weight of ~2 mg cm^{-2}. Mo foil was used as the cathode collector because it has remarkable stability far superior to Ni or Cu foils against corrosion in acidic ionic liquid electrolyte systems. Then the electrode was dried at 120 °C overnight in an oven to remove the residual NMP solvent. The electrolyte for RAIBs was prepared by mixing anhydrous $AlCl_3$ and [EMIm]Cl with a molar ratio of 1.3 : 1 in an Ar-filled glovebox, and then heated to 140 °C under stirring in the glovebox for 2 h and allowed to stand still for at least 12 h. 2032-type coin cells were fabricated by using the as-prepared cathode and metal Al foil anode (1.0 mm thick, 99.999%), and a cellulose acetate fiber paper separator. An additional Mo foil was placed between the cathode and the stainless steel shell of coin cells to prevent the etching of the shell. The amount of the electrolyte used in each cell was ~60 μL. CV and EIS analyses were performed with a CHI-760E electrochemical workstation. EIS curves were obtained in the frequency range between 100 kHz and 0.01 Hz with an applied amplitude of 5 mV. Galvanostatic charge–discharge curves and rate performance were measured on a multichannel battery test system (LAND CT2001A).

2.4. *Ex situ* characterization of Nb_2O_5 nanotube electrodes

For *ex situ* characterization, Swagelok cells were assembled with Nb_2O_5 nanotube cathodes, metal Al foil anodes and cell-

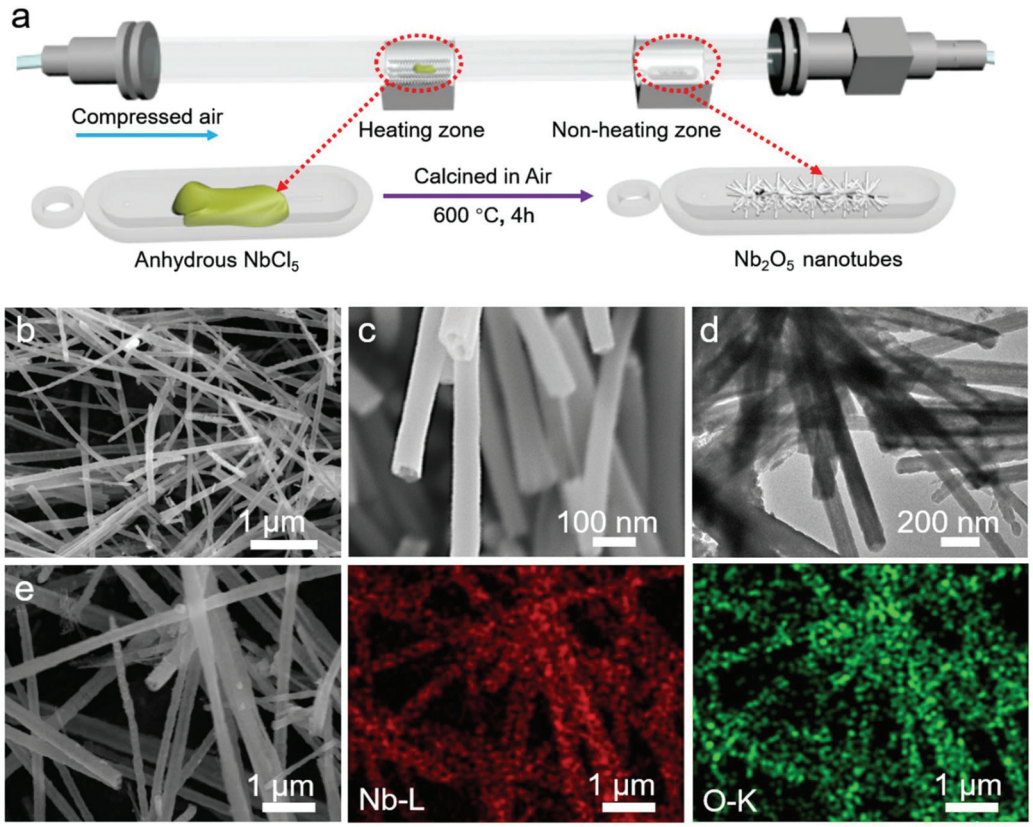

Fig. 1 Growth and microscopic characterization of monocrystalline Nb_2O_5 nanotubes. (a) Schematic illustration of the CVD growth of Nb_2O_5 nanotubes. (b and c) SEM images of Nb_2O_5 nanotubes. (d) TEM image of Nb_2O_5 nanotubes. (e) SEM image and the corresponding EDS elemental mapping (Nb and O elements) of Nb_2O_5 nanotubes.

ulose acetate fiber paper separators, similar to the coin cells. The Swagelok cells were charged and discharged at a current density of 25 mA g^{-1}. After the 1st cycle, the cells were disassembled in an Ar-filled glovebox in various charge–discharge states during the 2nd cycle. For *ex situ* XRD analysis, the cathode material was removed from the Swagelok cell and placed between two glass slides and then wrapped in Scotch tape, and moved out of the Ar-filled glovebox for XRD analysis. For *ex situ* HRTEM, HAADF-STEM and EDS analyses, the cathode material was removed from the Swagelok cell and dispersed in absolute alcohol, and then the mixture was added dropwise onto a copper grid, and moved out of the Ar-filled glovebox for the above-mentioned measurements. The exposure time in air was less than 20 min before the measurements.

3. Results and discussion

We developed an air-atmosphere chemical vapor deposition (CVD) method for growing Nb_2O_5 nanotubes, as schematically shown in Fig. 1a. Briefly, the anhydrous $NbCl_5$ powder was firstly sublimated to the gaseous state in the tube furnace and transferred to the downstream in a dry air flow, and then the nucleation and growth of Nb_2O_5 nanotubes was induced at a high temperature of 600 °C. Thus, agminated Nb_2O_5 nanotubes were grown in the non-heating zone at the downstream of the furnace without the need for any catalyst. Field-emission scanning electron microscopy (FE-SEM) and transmission electron microscopy (TEM) were used to characterize the microstructure of the as-prepared Nb_2O_5 nanotubes. SEM images (Fig. 1b and c) show that the Nb_2O_5 nanotubes are well defined with 200–300 nm diameter and 20–40 μm length. The TEM image (Fig. 1d) further confirms that the thickness of the nanotube wall is around 8–13 nm. Energy-dispersive X-ray spectrometry (EDS) elemental mapping (Fig. 1e) demonstrates the co-existence and uniform distribution of Nb and O elements in Nb_2O_5 nanotubes. The corresponding EDS spectrum and calculated element contents are shown in Fig. S1a,† and the data of commercial Nb_2O_5 powder measured at the same parameters are also provided in Fig. S1b.† For comparison, the SEM, high-angle annular dark-field scanning TEM (HAADF-STEM) and corresponding EDS elemental mapping analysis of commercial Nb_2O_5 powder are also provided in Fig. S2,† showing an irregular morphology with the size of several microns.

Further structural characterization of Nb_2O_5 nanotubes is shown in Fig. 2. High-resolution TEM (HRTEM, Fig. 2a and b) demonstrates that the exposed lattice planes are mainly the (001) facets and the growth orientation of Nb_2O_5 nanotubes is

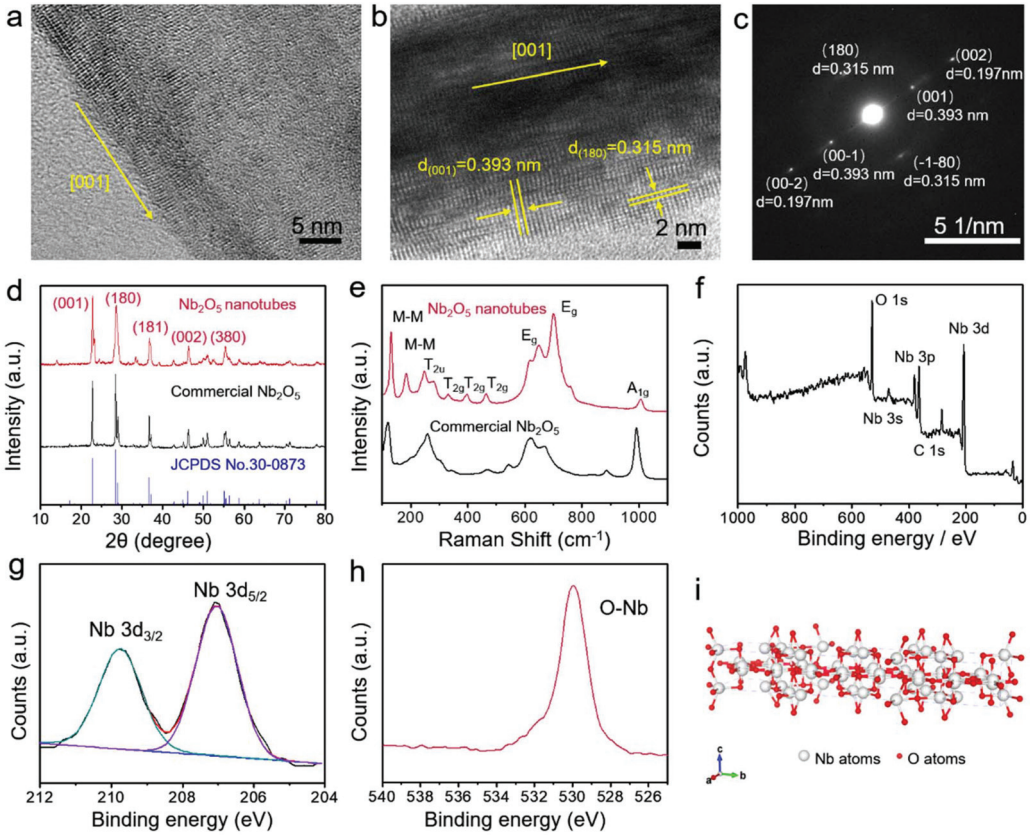

Fig. 2 Structural characterization of Nb_2O_5 nanotubes. (a and b) HRTEM images of Nb_2O_5 nanotubes. (c) shows a SAED pattern corresponding to (b). (d) XRD patterns and (e) Raman spectra of Nb_2O_5 nanotubes and commercial Nb_2O_5 powder. (f) Survey XPS spectrum of Nb_2O_5 nanotubes. (g and h) High-resolution XPS spectra at (g) Nb 3d and (h) O 1s regions of Nb_2O_5 nanotubes, respectively. (i) Schematic representation of the orthorhombic Nb_2O_5 crystal structure. White balls: Nb atoms; red balls: O atoms.

along the [001] direction. The lattice fringes of 0.393 nm and 0.315 nm can be indexed to the *d*-spacings of the (001) and (180) planes, respectively. Fig. 2c shows the corresponding selected area electron diffraction (SAED) pattern of Nb_2O_5 nanotubes, confirming that the nanotubes are single crystalline in nature. The calculated lattice fringes of 0.393 nm, 0.197 nm and 0.315 nm correspond to the *d*-spacings of the (001), (002) and (180) planes, respectively. The HRTEM images of commercial Nb_2O_5 powder are also provided in Fig. S3,† showing the same *d*-spacing of the (001) planes. X-ray diffraction (XRD) was used to characterize the phase and crystalline structure of the as-prepared Nb_2O_5 nanotubes (Fig. 2d). All the diffraction peaks are perfectly indexed to orthorhombic Nb_2O_5 with the following lattice parameters: a = 6.175 Å, b = 29.175 Å, c = 3.93 Å and $\alpha = \beta = \gamma = 90°$, which are well matched with the standard values (JCPDS no. 30-0873). The clear peaks in the XRD pattern confirm the formation of orthorhombic phase Nb_2O_5 nanotubes with high crystallinity. Remarkably, the intensity of the (001) peak at 22.6° is relatively enhanced because of the predominated (001) planes. Compared to commercial Nb_2O_5 powder, the intensity of the (001) peak of Nb_2O_5 nanotubes obviously increases, further indicating the exposure of more (001) planes and the preferred growth orientation along the [001] direction of Nb_2O_5 nanotubes.

The Raman spectra of Nb_2O_5 nanotubes and commercial Nb_2O_5 powder are compared in Fig. 2e. The strongest broad peak between 800 and 1000 cm^{-1} is the A_{1g} band, which corresponds to the longitudinal optical (LO) modes of the symmetrical Nb–O stretching (ν_1) associated with corner- and edge-shared NbO_6 octahedra.[60] The shoulder peak in the range of 600–700 cm^{-1} corresponds to the ν_2 (E_g) band and transverse optical (TO) modes. The weak peaks observed between 300 and 560 cm^{-1} are designated to the ν_5 (T_{2g}) modes and the fingerprint peaks observed in the range of 200–300 cm^{-1} are assigned to the T_{2u} modes. A sharp and strong peak at around 140 cm^{-1} is assigned to the metal–metal (Nb–Nb) vibration mode. The shifting of the A_{1g} band from ~991 cm^{-1} (for commercial Nb_2O_5 powder) to ~1005 cm^{-1} (for Nb_2O_5 nanotubes) and the intensity decay indicate that the ratio of edge-shared octahedra in Nb_2O_5 nanotubes is less than that in commercial Nb_2O_5 powder, which might arise from the high specific surface area of the nanotube morphology. The A_{1g} band of corner-shared NbO_6 octahedra (~886 cm^{-1} for commercial Nb_2O_5 powder) disappeared in Nb_2O_5 nanotubes, suggesting that the presence of this structure in Nb_2O_5 nanotubes is much less than that in commercial Nb_2O_5 powder. The bands observed at 618 cm^{-1} and 670 cm^{-1} in commercial Nb_2O_5 powder might be ascribed to the an-

isotropy of the NbO_6 octahedra; the corresponding bands in Nb_2O_5 nanotubes are shifted to 648 cm^{-1} and 702 cm^{-1} with enhanced intensities, suggesting that the anisotropy of Nb_2O_5 nanotubes is stronger than that of commercial Nb_2O_5 powder with a bulky morphology. The clearer spectral peaks of T_{2g} (330–550 cm^{-1}), T_{2u} (200–303 cm^{-1}) and M–M (132 cm^{-1} and 184 cm^{-1}) bands of Nb_2O_5 nanotubes might be attributed to the rapid crystallization process. X-ray photoelectron spectroscopy (XPS) was performed to further detect the surface elemental compositions and chemical states of Nb_2O_5 nanotubes. The survey XPS spectrum (Fig. 2f) shows the clear presence of O 1s, Nb 3s, Nb 3p and Nb 3d peaks. Fig. 2g shows the high-resolution XPS spectrum at the Nb 3d region, showing two peaks at 209.7 and 206.9 eV, respectively, corresponding to the Nb $3d_{3/2}$ and Nb $3d_{5/2}$ bands. In the O 1s region (Fig. 2h), the peak centered at 530.6 eV originated from the O–Nb bonds. Based on the above characterization, the crystal structure of orthorhombic phase Nb_2O_5 nanotubes with the space group of *Pbam*55 can be verified, as shown in Fig. 2i.

The electrochemical performances of Nb_2O_5 nanotubes as a cathode material in the coin cells of RAIBs were evaluated within the voltage range of 0.1–2.0 V (Fig. 3). The areal loading weight of Nb_2O_5 nanotubes is kept at ~2 mg cm^{-2}. A mixture of $AlCl_3$ and [EMIm]Cl with a molar ratio of 1.3 : 1 was used as the electrolyte, and metal Al foil was used as the anode, as detailed in the Experimental section of the ESI.† Fig. 3a and b show the charge–discharge curves of RAIBs based on the cathodes of Nb_2O_5 nanotubes and commercial Nb_2O_5 powder during the initial two cycles at a current density of 25 mA g^{-1} and a temperature of 25 °C. Interestingly, the charge/discharge capacities in the 2nd cycle are larger than those in the 1st cycle, indicating the process of electrode activation. During the 1st

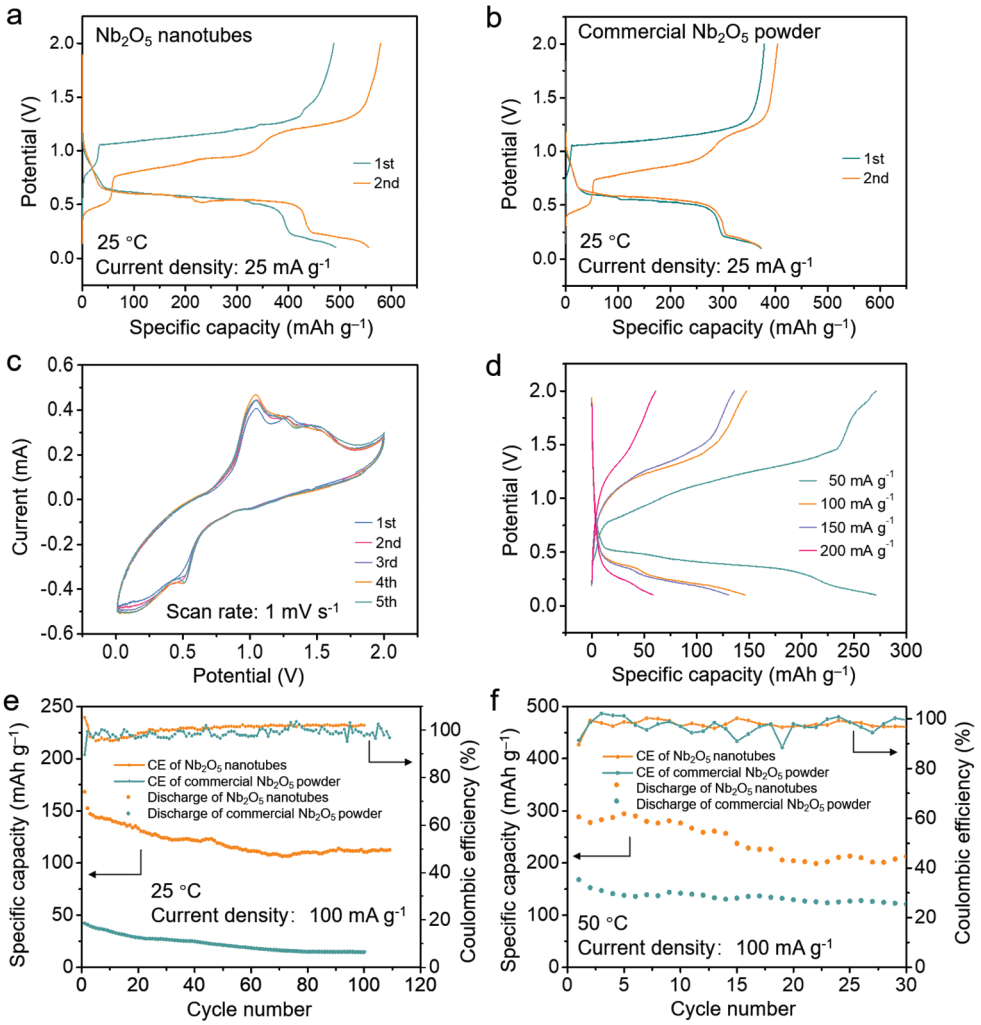

Fig. 3 Electrochemical performances of Nb_2O_5 nanotubes in RAIBs. (a and b) Galvanostatic charge–discharge profiles of (a) Nb_2O_5 nanotubes and (b) commercial Nb_2O_5 powder at a current density of 25 mA g^{-1} and a temperature of 25 °C. (c) CV curves and (d) rate performance of the Nb_2O_5 nanotube-based electrode in RAIBs at 25 °C. (e) Cycling performances and coulombic efficiencies of the RAIBs assembled with the cathodes of Nb_2O_5 nanotubes and commercial Nb_2O_5 powder at a current density of 100 mA g^{-1} and a temperature of 25 °C. (f) Cycling performances of the RAIBs assembled with the cathodes of Nb_2O_5 nanotubes and commercial Nb_2O_5 powder at a current density of 100 mA g^{-1} and an elevated temperature of 50 °C.

charging process, the electrode of Nb_2O_5 nanotubes exhibited two clear charge voltage plateaus in the range of 1.06–1.21 V and 1.25–1.31 V, while in the 2nd cycle, obvious charge voltage plateaus in the range of 0.76–0.96 V and 1.16–1.32 V were observed. These might be attributed to the staging mechanism of the intercalation of $AlCl_4^-$ ions into the Nb_2O_5 lattice[65] combined with the formation of a solid–electrolyte interface (SEI) layer during the 1st charging process.[23] During the discharging process, the plateaus between 0.66–0.52 V and 0.23–0.15 V could be attributed to the staging mechanism of the deintercalation of $AlCl_4^-$ ions from the Nb_2O_5 lattice. The Nb_2O_5 nanotubes showed the charge–discharge plateaus similar to those of commercial Nb_2O_5 powder, indicating that the same electrochemical reactions occurred. The discharge capacity of Nb_2O_5 nanotubes during the 1st cycle is 492 mA h g^{-1}, respectively, much higher than that of Nb_2O_5 powder (372 mA h g^{-1}). The coulombic efficiency (CE) of Nb_2O_5 nanotubes during the 1st cycle is nearly 100%, also higher than that of commercial Nb_2O_5 powder (98.15%). The discharge capacity of Nb_2O_5 nanotubes during the 2nd cycle increased to 556 mA h g^{-1} and the CE is still higher than 98%, better than those of commercial Nb_2O_5 powder (386 mA h g^{-1} and 94%, respectively). As shown inFig. 3c, cyclic Cyclic voltammetry (CV) tests were performed to characterize the electrochemical behavior of Nb_2O_5 nanotubes by pairing with the metal Al anode at a scan rate of 1 mV s^{-1} within a voltage window from 0.01 to 2.0 V. In the 1st anodic scan, the weak peak at 1.25 V and the strong peak at ~1.06 V were attributed to the insertion of $AlCl_4^-$ ions, which can be further verified by *ex situ* STEM and EDS elemental mapping. In the cathodic scans, the peaks centered at around ~0.55 V could match with the discharge voltage plateaus in Fig. 3a and b. The good repeatability of CV curves indicates that the RAIBs based on Nb_2O_5 nanotubes might have good cycling stability. The rate performance of Nb_2O_5 nanotubes was also examined (Fig. 3d), which is much superior to that of commercial Nb_2O_5 powder (Fig. S4†). The assembled RAIBs using Nb_2O_5 nanotubes as a cathode material were tested at current densities from 50 to 500 mA g^{-1}. When the current density was set to 50 mA g^{-1}, the discharge capacity reached ~270 mA h g^{-1}. When the current density increased to 100 and 150 mA g^{-1}, the RAIBs based on Nb_2O_5 nanotubes still exhibit discharge capacities of 147 and 136 mA h g^{-1}, respectively. However, when the current density further increased to 200 mA g^{-1}, the capacity decreased rapidly, possibly owing to the inherent drawback of slow kinetics between the interface of the ion liquid electrolyte and the metal oxide electrode. The room temperature cycling performance of the RAIBs based on Nb_2O_5 nanotubes at a current density of 100 mA g^{-1} is shown in Fig. 3e. The cell can work stably for over 110 cycles with an average CE of nearly 100% and a capacity retention of ~113 mA h g^{-1}. The discharge capacity and cycling performance of Nb_2O_5 nanotubes are much better than those of commercial Nb_2O_5 powder (Fig. 3e), which can be attributed to the high utilization ratio of the active material originated from the shorter ion diffusion pathway and higher porosity of Nb_2O_5 nanotubes. This result can be further explained by the electrochemistry impedance spectra (EIS, Fig. S5†), which shows that the electrode based on Nb_2O_5 nanotubes possesses lower charge-transfer resistance than commercial Nb_2O_5 powder. Interestingly, we also tested the galvanostatic charge–discharge performance of Nb_2O_5 nanotube-based RAIBs at an elevated temperature of 50 °C (Fig. 3f). The discharge capacity of Nb_2O_5 nanotubes increased to ~290 mA h g^{-1} at the initial cycles under a current density of 100 mA g^{-1} at 50 °C, and it was still maintained at ~213 mA h g^{-1} after 30 cycles. The discharge capacity of commercial Nb_2O_5 powder was also increased to ~140 mA h g^{-1} under 100 mA g^{-1} at 50 °C. The improved capacity retention of Nb_2O_5 nanotubes superior to Nb_2O_5 powder at elevated temperatures could be ascribed to the better ion transfer kinetics and higher active material utilization of Nb_2O_5 nanotubes.[66,67] The Nb_2O_5 nanotubes with thin walls and hollow inner spaces could further facilitate the ion transfer and thus are more beneficial for high-temperature performances. Therefore, the Nb_2O_5 nanotubes exhibit competitive electrochemical performances compared to the other transition metal oxide- or sulfide-based cathode materials for RAIBs reported in previous literature (Table S1†).[15,23,34–40]

To further study the energy storage mechanism of Nb_2O_5 nanotubes in RAIBs, Swagelok cells with Nb_2O_5 nanotubes as the cathode and metal Al foil as the anode were assembled for detailed *ex situ* characterization. *Ex situ* XRD analysis was used to analyze the crystalline structural variations of Nb_2O_5 nanotubes during the charge–discharge processes (Fig. 4a and b). The broad shoulder peaks at around 25° are derived from acetylene black used as the conductive additive in the electrodes. The XRD peak intensities of acetylene black are almost unchanged during the repeated charge/discharge processes; however, the peak intensities of Nb_2O_5 are changed periodically owing to the reversible intercalation/deintercalation of $AlCl_4^-$ ions. In the initial state (before the test, point 1 in Fig. 4a), the XRD pattern (Fig. 4b, line 1) shows clear diffraction peaks, and the (001) peak at 22.6° has the strongest intensity. When charged to 2.0 V in the 1st cycle (Fig. 4a, point 2), the crystallinity of Nb_2O_5 nanotubes (Fig. 4b, line 2) decreased, and the intensity of the (001) peak diminished when compared to that of the (180) peak. After being fully discharged to 0.1 V (Fig. 4b, line 3), the (001) peak turned back to the strongest diffraction peak. When recharged to 0.8 V in the 2nd cycle (Fig. 4a, point 4), the intensity of the (001) peak (Fig. 4b, line 4) is comparable to that of the (180) peak. After being recharged to 2.0 V (Fig. 4a, point 5), the intensity of the (001) peak further decreased and the (180) peak became the strongest peak (Fig. 4b, line 5). During the discharge process to 0.7 V (Fig. 4a, point 6), the relative intensity of the (001) peak increased again compared to that of the (180) peak (Fig. 4b, line 6). When fully discharged to 0.1 V (Fig. 4a, point 7), the intensity of the (001) peak recovered and became the strongest peak again (Fig. 4b, line 7). These results indicate the occurrence of reversible insertion/extraction of $AlCl_4^-$ ions in/from the crystalline lattice of Nb_2O_5 nanotubes. The TEM and HRTEM images of Nb_2O_5 nanotubes in the fully charged state are also shown in Fig. 4c–e. It can be observed that the Nb_2O_5

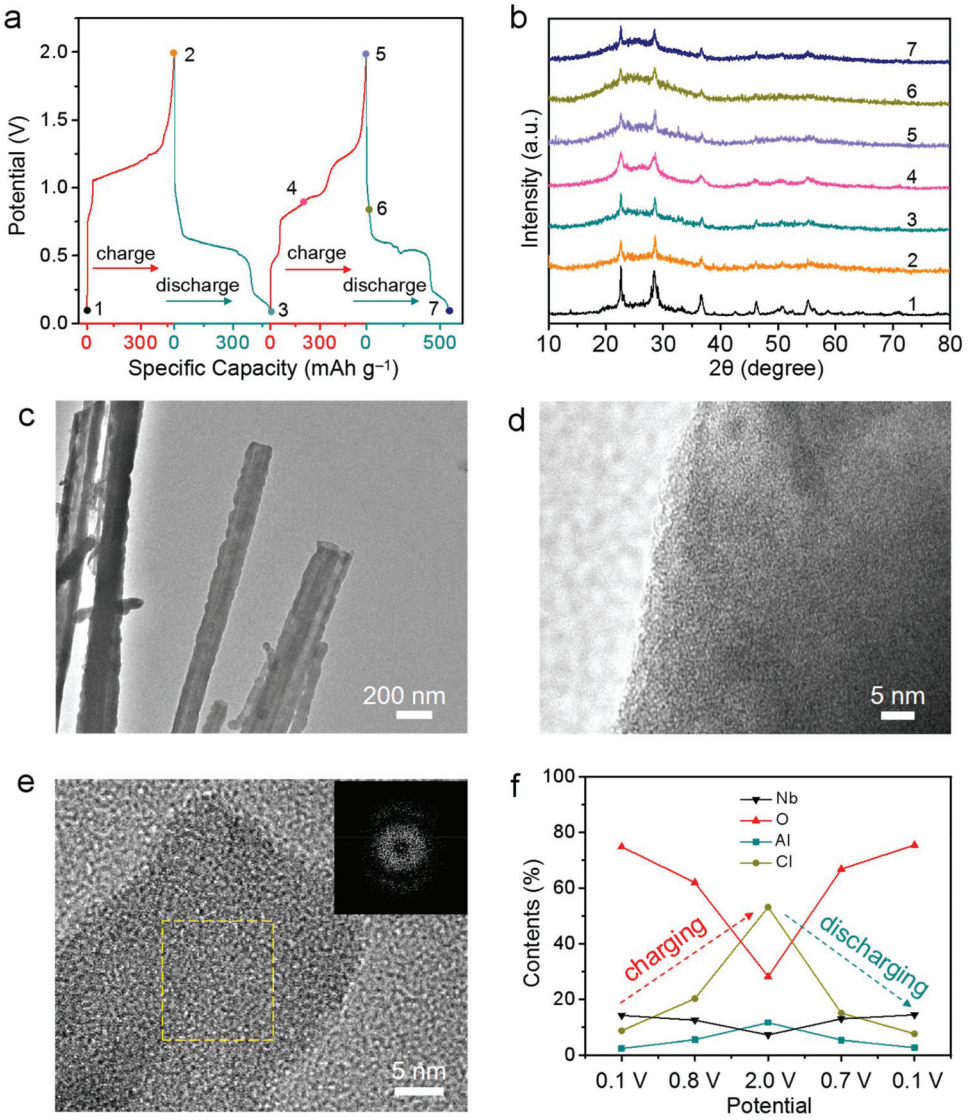

Fig. 4 *Ex situ* characterization of Nb_2O_5 nanotubes after battery tests. (a) Galvanostatic charge–discharge voltage profiles of Nb_2O_5 nanotubes at a current density of 25 mA g^{-1}. The points labeled with 1 to 7 indicate the different discharge–charge states in which the XRD patterns in (b) were collected. (b) *Ex situ* XRD patterns of the Nb_2O_5 nanotube electrode collected at the initial 2 cycles in various discharge–charge states. (c) TEM and (d and e) HRTEM images of fully charged Nb_2O_5 nanotubes after 2 cycles. The inset in e shows the corresponding FFT pattern. (f) The variations of elemental contents in the Nb_2O_5 nanotube electrode in various discharge–charge states measured by EDS analysis.

nanotubes in the fully charged state exhibit low crystallinity, indicating that the intercalation of $AlCl_4^-$ ions could reversibly reduce the periodicity of the Nb_2O_5 crystal structure. The TEM and HRTEM images of fully discharged Nb_2O_5 nanotubes after 2 cycles (Fig. S6†) show almost no change in the crystalline structure, indicating the reversible $AlCl_4^-$ insertion/extraction and well-maintained structural integrity of Nb_2O_5 nanotubes.

To verify the intercalation/deintercalation mechanism of $AlCl_4^-$ ions in Nb_2O_5 nanotubes, EDS analysis and *ex situ* STEM characterization were performed during the 2nd cycle at a current density of 25 mA g^{-1}. The elemental contents measured by EDS analysis in different charge–discharge states are shown in Fig. 4f, revealing the reversible elemental content variations of Al and Cl species induced by the intercalation/deintercalation of $AlCl_4^-$ ions. Fig. 5 also shows the *ex situ* HAADF-STEM images and the corresponding spatial elemental mappings of Nb_2O_5 nanotubes in different charge–discharge states. Fig. 5a shows the presence of residual Al and Cl elements after the discharge process of the 1st cycle, indicating the incomplete deintercalation of $AlCl_4^-$ ions in the fully discharged state. Fig. 5b–e show the elemental distributions after charging to 0.8 V and 2.0 V, and then discharging to 0.7 V and 0.1 V, respectively. Overall, the HAADF-STEM images show the even distribution of Nb, O, Al and Cl elements in the Nb_2O_5 nanotubes, suggesting that the insertion of $AlCl_4^-$ ions happened inside the nanotubes rather than only on the surface.

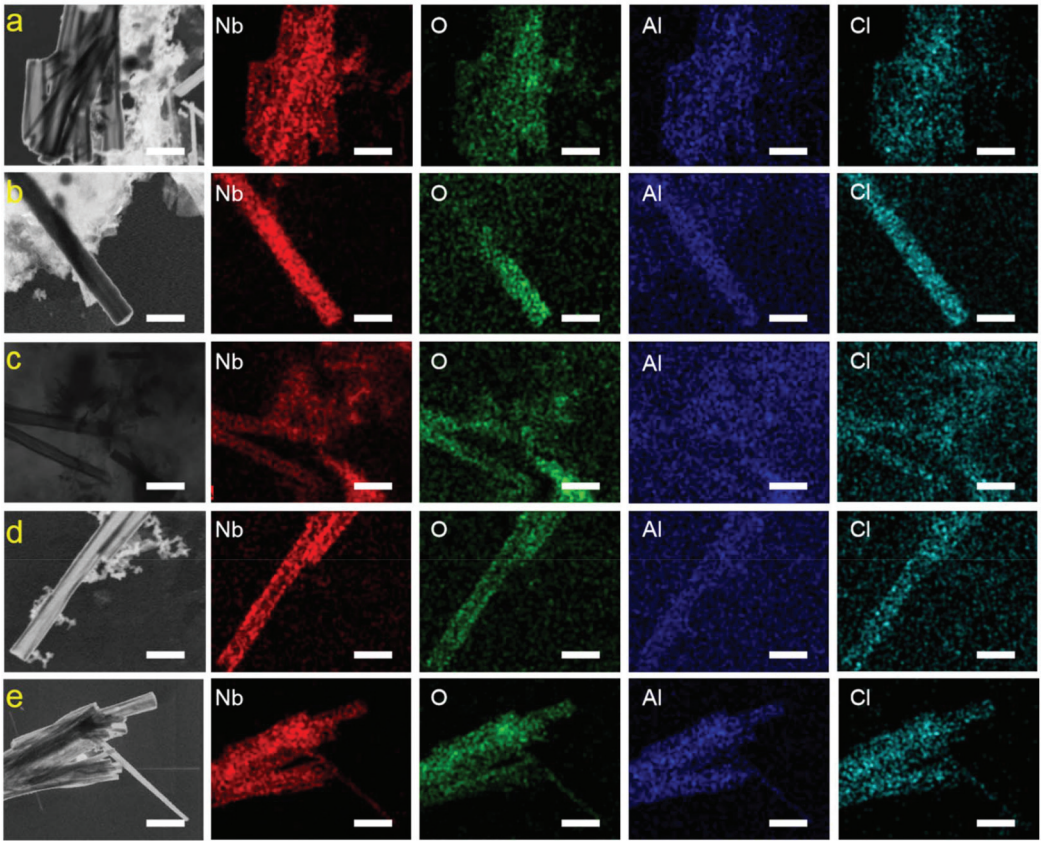

Fig. 5 *Ex situ* HAADF-STEM images and the corresponding elemental mappings of Nb_2O_5 nanotubes in different charge–discharge states during the 2nd cycle: (a) the initial state (fully discharged to 0.1 V); (b) partially charged to 0.8 V; (c) fully charged to 2.0 V; (d) partially discharged to 0.7 V; (e) fully discharged to 0.1 V. Scale bar: 500 nm.

4. Conclusions

In summary, we have developed an efficient CVD approach to grow monocrystalline Nb_2O_5 nanotubes as a novel cathode material for RAIBs. Structural characterization suggests that the dominant lattice planes of Nb_2O_5 nanotubes are mainly the (001) planes. The as-synthesized Nb_2O_5 nanotubes exhibit high specific capacity and high reversible stability in RAIBs at room temperature or even at 50 °C., much superior to those of commercial Nb_2O_5 powder. Detailed *ex situ* characterization in different charge–discharge states reveals that the electrochemical energy storage mechanism involves a reversible $AlCl_4^-$ insertion/extraction into/from single-crystal Nb_2O_5 nanotubes. Benefiting from the advantageous nanostructural features of Nb_2O_5 nanotubes with a short ion diffusion distance originated from the thin tube walls, hollow inner spaces and high porosity, the Nb_2O_5 nanotubes exhibit improved kinetics, good rate performance and a high utilization ratio in RAIBs. This study suggests that the structure and morphology modulation of transition metal compounds as high-performance electrode materials is a promising strategy for realizing advanced multivalent ion batteries.

Conflicts of interest

There are no conflicts to declare.

Acknowledgements

This work was supported by the National Key R&D Program (2017YFA0208200, 2016YFB0700600), the Fundamental Research Funds for the Central Universities (0205-14380219), the Projects of NSFC (21872069, 51761135104, 21573108), the Natural Science Foundation of Jiangsu Province (BK20180008, BK20170644), and the High-Level Innovation and Entrepreneurship Project of Jiangsu Province of China.

References

1 J. M. Tarascon and M. Armand, *Nature*, 2011, **414**, 359–367.
2 M. Armand and J. M. Tarascon, *Nature*, 2008, **451**, 652–657.
3 Z. Yang, *Chem. Rev.*, 2011, **111**, 3577–3613.
4 J. Goodenough, *J. Solid State Electrochem.*, 2012, **16**, 2019–2029.

5 D. Larcher and J. M. Tarascon, *Nat. Chem.*, 2015, **7**, 19–29.
6 J. B. Goodenough and K. S. Park, *J. Am. Chem. Soc.*, 2013, **135**, 1167–1176.
7 Y. Hu, T. Zhang, F. Cheng, Q. Zhao, X. Han and J. Chen, *Angew. Chem., Int. Ed.*, 2015, **54**, 4338–4343.
8 Y. K. Sun, S. T. Myung, B. C. Park, J. Prakash, I. Belharouak and K. Amine, *Nat. Mater.*, 2009, **8**, 320–324.
9 F. Ambroz, T. J. Macdonald and T. Nann, *Energy Mater.*, 2017, **7**, 1602093.
10 G. A. Elia, K. Marquardt, K. Hoeppner, S. Fantini, R. Lin, E. Knipping, W. Peters, J. F. Drillet, S. Passerini and R. Hahn, *Adv. Mater.*, 2016, **28**, 7564–7579.
11 S. W. Kim, D. H. Seo, X. Ma, G. Ceder and K. Kang, *Adv. Energy Mater.*, 2012, **2**, 710–721.
12 T. Wu, C. Zhang, H. Hou, P. Ge, G. Zou, W. Xu, S. Li, Z. Huang, T. Guo, M. Jing and X. Ji, *Adv. Funct. Mater.*, 2018, 1705744.
13 T. Ichitsubo, T. Adachi, S. Yagi and T. Doi, *J. Mater. Chem.*, 2011, **21**, 11764–11772.
14 N. Singh, T. S. Arthur, C. Ling, M. Matsui and F. Mizuno, *Chem. Commun.*, 2013, **49**, 149–151.
15 T. Koketsu, J. Ma, B. J. Morgan, M. Body, C. Legein, W. Dachraoui, M. Giannini, A. Demortière, M. Salanne, F. Dardoize, H. Groult, O. J. Borkiewicz, K. W. Chapman, P. Strasser and D. Dambournet, *Nat. Mater.*, 2017, **16**, 1142–1148.
16 C. Xu, B. Li, H. Du and F. Kang, *Angew. Chem., Int. Ed.*, 2012, **51**, 933–935.
17 L. Zhang, L. Chen, X. Zhou and Z. Liu, *Adv. Energy Mater.*, 2015, **5**, 1400930.
18 M. S. Chae, J. W. Heo, H. H. Kwak, H. Lee and S. T. Hong, *J. Power Sources*, 2017, **337**, 204–211.
19 C. D. Wessells, S. V. Peddada, R. A. Huggins and Y. Cui, *Nano Lett.*, 2011, **11**, 5421–5425.
20 D. Su, A. McDonagh, S. Z. Qiao and G. Wang, *Adv. Mater.*, 2017, **29**, 1604007.
21 P. Padigi, G. Goncher, D. Evans and R. Solanki, *J. Power Sources*, 2015, **273**, 460–464.
22 T. Tojo, Y. Sugiura, R. Inadab and Y. Sakurai, *Electrochim. Acta*, 2016, **207**, 22–27.
23 S. Wang, S. Jiao, J. Wang, H. S. Chen, D. Tian, H. Lei and D. N. Fang, *ACS Nano*, 2017, **11**, 469–477.
24 P. R. Gifford and J. B. Palmisano, *J. Electrochem. Soc.*, 1998, **135**, 650–654.
25 H. Jiao, C. Wang, J. Tu, D. Tian and S. Jiao, *Chem. Commun.*, 2017, **53**, 2331.
26 D. Y. Wang, C. Y. Wei, M. C. Lin, C. J. Pan, H. L. Chou, H. A. Chen, M. Gong, Y. Wu, C. Yuan, M. Angell, Y. J. Hsieh, Y. H. Chen, C. Y. Wen, C. W. Chen, B. J. Hwang, C. C. Chen and H. J. Dai, *Nat. Commun.*, 2017, **8**, 14283.
27 J. V. Raniz, V. Kanakaiah, T. Dadmal, M. S. Rao and S. Bhavanarushi, *J. Electrochem. Soc.*, 2017, 160.
28 H. Chen, F. Guo, Y. Liu, T. Huang, B. Zheng, N. Ananth, Z. Xu, W. Gao and C. Gao, *Adv. Mater.*, 2017, 29.
29 H. Chen, H. Xu, S. Wang, T. Huang, J. Xi, S. Cai, F. Guo, Z. Xu, W. Gao and C. Gao, *Sci. Adv.*, 2017, **3**, 7233.
30 M. C. Lin, M. Gong, B. Lu, Y. Wu, D. Y. Wang, M. Guan, M. Angell, C. Chen, J. Yang, B. J. Hwang and H. Dai, *Nature*, 2015, **520**, 325–328.
31 Y. Wu, M. Gong and M. C. Lin, *Adv. Mater.*, 2016, **28**, 9218–9222.
32 X. Yu, B. Wang, D. Gong, Z. Xu and B. Lu, *Adv. Mater.*, 2017, 29.
33 N. Jayaprakash, S. K. Das and L. A. Archer, *Chem. Commun.*, 2011, **47**, 12610.
34 H. Wang, Y. Bai, S. Chen, X. Luo, C. Wu, F. Wu, J. Lu and K. Amine, *ACS Appl. Mater. Interfaces*, 2015, **7**, 80–84.
35 M. Chiku, H. Takeda, S. Matsumura, E. Higuchi and H. Inoue, *ACS Appl. Mater. Interfaces*, 2015, **7**, 24385–24389.
36 W. Wang, B. Jiang, W. Xiong, H. Sun, Z. Lin, L. Hu, J. Tu, J. Hou, H. Zhu and S. Jiao, *Sci. Rep.*, 2013, **3**, 3383.
37 W. Kaveevivitchai, A. Huq, S. Wang, M. J. Park and A. Manthiram, *Small*, 2017, **13**, 1701296.
38 Z. Li, B. Niu, J. Liu, J. Li and F. Kang, *ACS Appl. Mater. Interfaces*, 2018, **10**, 9451–9459.
39 S. Wang, Z. Yu, J. Tu, J. Wang, D. Tian, Y. Liu and S. Jiao, *Adv. Energy Mater.*, 2016, **6**, 1600137.
40 L. Geng, G. Lv, X. Xing and J. Guo, *Chem. Mater.*, 2015, **27**, 4926–4929.
41 Y. Hu, D. Ye, B. Luo, H. Hu, X. Zhu, S. Wang, L. Li, S. Peng and L. Wang, *Adv. Mater.*, 2018, 30.
42 Z. Yu, Z. Kang, Z. Hu, J. Lu, Z. Zhou and S. Jiao, *Chem. Commun.*, 2016, **52**, 10427.
43 P. G. Pickup and R. A. Osteryoung, *J. Am. Chem. Soc.*, 1984, **106**, 2294–2299.
44 L. Janiszewska and R. A. Osteryoung, *J. Electrochem. Soc.*, 1987, **134**, 2787–2794.
45 J. Tang and R. A. Osteryoung, *Synth. Met.*, 1991, **44**, 307–319.
46 L. M. Goldenberg and R. A. Osteryoung, *Synth. Met.*, 1994, **64**, 63–68.
47 N. S. Hudak, *J. Phys. Chem. C*, 2014, **118**, 5203–5215.
48 G. Cohn, L. Ma and L. A. Archer, *J. Power Sources*, 2015, **283**, 416–422.
49 T. Gao, X. Li, X. Wang, J. Hu, F. Han, X. Fan, L. Suo, A. J. Pearse, S. B. Lee, G. W. Rubloff, K. J. Gaskell, M. Noked and C. Wang, *Angew. Chem., Int. Ed.*, 2016, **128**, 10052–10055.
50 H. Yang, L. Yin, J. Liang, Z. Sun, Y. Wang, H. Li, K. He, L. Ma, Z. Peng, S. Qiu, C. Sun, H. M. Cheng and F. Li, *Angew. Chem., Int. Ed.*, 2018, **57**, 1898–1902.
51 H. Tian, S. Zhang, Z. Meng, W. He and W. Q. Han, *ACS Energy Lett.*, 2017, **2**, 1170–1176.
52 M. Y. Song, N. R. Kim, H. J. Yoon, S. Y. Cho, H. J. Jin and Y. S. Yun, *ACS Appl. Mater. Interfaces*, 2017, **9**, 2267–2274.
53 B. Deng, T. Lei, W. Zhu, L. Xiao and J. Liu, *Adv. Funct. Mater.*, 2018, **28**, 1704330.
54 F. Liu, X. Cheng, R. Xu, Y. Wu, Y. Jiang and Y. Yu, *Adv. Funct. Mater.*, 2018, **28**, 1800394.
55 X. Wang, Q. Li, L. Zhang, Z. Hu, L. Yu, T. Jiang, C. Lu, C. Yan, J. Sun and Z. Liu, *Adv. Mater.*, 2018, **30**, 1800963.

56 H. Yang, R. Xu, Y. Gong, Y. Yao, L. Gu and Y. Yu, *Nano Energy*, 2018, **48**, 448–455.
57 D. Chen, J. H. Wang, T. F. Chou and B. Zhao, *J. Am. Chem. Soc.*, 2017, **139**, 7071–7081.
58 X. Wang, G. Li, R. Tjandra, X. Fan, X. Xiao and A. Yu, *RSC Adv.*, 2015, **5**, 41179–41185.
59 L. Yang, Y. E. Zhu, J. Sheng, F. Li, B. Tang, Y. Zhang and Z. Zhou, *Small*, 2017, **13**, 1702588.
60 B. Varghese, S. C. Haur and C. T. Lim, *J. Phys. Chem. C*, 2008, **112**, 10008–10012.
61 M. Lübke, A. Sumboja, I. Johnson, D. J. L. Brett, P. R. Shearing and Z. Liu, *Electrochim. Acta*, 2016, **192**, 363–369.
62 J. Y. Cheong, C. Kim, J. W. Jung, K. R. Yoon and I. D. Kim, *Small*, 2017, **13**, 1603610.
63 L. Yan, X. Rui, G. Chen, W. Xu and H. Luo, *Nanoscale*, 2016, **8**, 8443–8465.
64 L. Li, J. Deng, R. Yu, J. Chen, Z. Wang and X. Xing, *J. Mater. Chem. A*, 2013, **1**, 11894.
65 P. Bhauriyal, A. Mahata and B. Pathak, *Phys. Chem. Chem. Phys.*, 2017, **19**, 7980–7989.
66 W. Kaveevivitchai, A. Huq and S. Wang, *Small*, 2017, **13**, 1701296.
67 H. Chen, H. Xu, S. Wang, T. Huang, J. Xi, S. Cai, F. Guo, Z. Xu, W. Gao and C. Gao, *Sci. Adv.*, 2017, **3**, 7233.